





RESEARCH ARTICLE OPEN ACCESS

Surface Passivation of Silicon Nanoparticles Monitored by In Situ FTIR

Maren Dworschak¹  | Martin Müller²  | Tim Tjardts³  | Lorenz Kienle^{2,4} | Jan Benedikt^{1,4} 

¹Department of Experimental and Applied Physics, Group of Experimental Plasma Physics, Kiel University, Kiel, Germany | ²Department of Material Science, Group of Synthesis and Real Structure, Kiel University, Kiel, Germany | ³Department of Material Science, Chair of Multicomponent Materials, Kiel University, Kiel, Germany | ⁴Kiel Nano, Surface and Interface Science KiNSIS, Kiel University, Kiel, Germany

Correspondence: Jan Benedikt (benedikt@physik.uni-kiel.de)

Received: 2 September 2024 | **Revised:** 29 October 2024 | **Accepted:** 21 November 2024

Funding: This study was supported by German Research Foundation (DFG, project number 426208229) and Major Research Instrumentation Program projects (INST 257/595-1 and INST 257/704-1).

Keywords: atmospheric pressure plasmas | FTIR | in situ | nanoparticles | silane | silicon | surface passivation | TEM | XPS

ABSTRACT

A setup consisting of two atmospheric plasma sources is used for the combined synthesis and passivation of nanoparticles. The silicon nanoparticles synthesized in the first source are analyzed for their chemical composition, morphology, and photoluminescence. The particles are then treated with a second plasma to induce surface passivation. The passivation process of the particles is monitored in real time using in situ infrared absorption spectroscopy. The results indicate that this treatment induces methylation of the silicon nanocrystals, which is further supported by XPS analysis. This surface passivation shifts the maximum of the photoluminescent signal to blue in the visible spectral region. Further optimization of the reported nanoparticle passivation process can provide a flexible tool for tuning nanoparticle properties.

1 | Introduction

Silicon nanoparticles (Si-NPs) and nanocrystals (Si-NCs) have gained significant attention in both scientific and industrial areas due to their unique properties and versatile applications. Si-NCs possess advantageous characteristics such as biocompatibility, biodegradability, and non-toxicity [1–3], making them promising candidates for various biomedical applications, including drug delivery and biomedical imaging [4, 5]. The tunable optical and electrical properties of Si-NCs, influenced by their size and surface termination [6], give them the prerequisites for the development of light-emitting devices [7], photovoltaics [8], and sensors [9, 10]. Surface passivation and functionalization resulting in the desired surface termination play a crucial role in modulating the photoluminescence (PL) intensity, quantum yield, as well as stability of Si-NPs. Non-thermal equilibrium plasmas operated at atmospheric pressure offer great flexibility in applications that are commonly carried

out by low-pressure vacuum systems [11, 12]. This includes the synthesis of optical-quality Si-NPs or silicon quantum dots [13]. These nanoparticles typically possess highly sensitive surfaces and are susceptible to alterations in their properties over time due to aging. Moreover, surface modification of nanoparticles is often needed to improve the optical properties. The work of Kúsová et al. has shown that methyl groups bonded to the nanocrystal surface enhance the PL properties of Si-NPs significantly [14]. The electrochemically etched Si-NC powder dispersed in a solvent from a mixed aromatic hydrocarbon solution was irradiated with a UV laser. The original PL band at ~600–650 nm and a decay time of around 20 ms was replaced by a new rapidly decaying yellow band comparable to the PL of direct band gap materials. Organic residues attached to the Si-NC surface via both Si-C and Si-O-C bonds were found; however, the exact chemical mechanism remains unknown due to the complexity of the experiment. Further, it has been theoretically shown that passivation with methane can tune the

This is an open access article under the terms of the [Creative Commons Attribution-NonCommercial-NoDerivs](https://creativecommons.org/licenses/by-nc-nd/4.0/) License, which permits use and distribution in any medium, provided the original work is properly cited, the use is non-commercial and no modifications or adaptations are made.

© 2024 The Author(s). *Plasma Processes and Polymers* published by Wiley-VCH GmbH.

optical band gap of ultra-small (< 3 nm) nanoparticles [15]. The methyl groups attached to the surface of Si-NCs introduce a tensile strain in the particles, leading to an increase in the band gap and consequently blue-shifting the maximum of the PL signal. This passivation is supposedly also connected to an increase in the overall PL intensity. The analysis of the particle composition of both passivated and pristine particles can be carried out by various methods. Fourier Transformed Infrared Absorption spectroscopy (FTIR) is one of the preferred measurement techniques. To analyze the material generated in a plasma, the material is usually deposited on a substrate and then brought into the sample compartment of the FTIR spectrometer. In most cases, this will automatically expose the sample to ambient humid air and set off oxidation of the material. Oxidized functional groups could then be falsely identified to have their origin in the synthesis process.

In this paper, we report on a double atmospheric pressure plasma system with the combined synthesis of quantum dots in the first, and their modification in the second atmospheric pressure plasma source. A similar approach has been used already for low-pressure systems by other groups, such as Kortshagen et al., where one reactor was responsible for the particle generation and the second one for subsequent etching [16] or surface passivation [17]. A rather complicated double atmospheric process for the generation and treatment of nanoparticles has also been reported, for example, by Boies et al. [18]. In our work, the material properties and gas phase consumption of molecular precursors are monitored in situ using a reflective FTIR setup. The optical and other properties of the Si-NPs have been studied ex situ using transmission electron microscopy (TEM), and their photoluminescent properties related to surface passivation have been characterized.

2 | Experimental Setup and Diagnostics

2.1 | Plasma Sources

Synthesis and surface passivation of Si-NPs are performed separately in a two-step process in two similarly looking atmospheric pressure plasma jets that are connected in series. Both atmospheric plasma jets used in this publication are downsized versions of the HelixJet first published by Schäfer et al. in 2019 [19]. For the combined synthesis and passivation of the nanoparticles, two HelixJets are placed on top of each other. As seen in Figure 1 on the left, these jets consist of a quartz glass capillary with an outer diameter of 5 mm and a wall thickness of 1 mm. A set of helical electrodes is placed around each jet in a double helix structure. The electrodes cover the capillary in a length of 4 cm. One of each of the electrodes is grounded, while the other one is driven by a 13.56 MHz frequency. Both jets are connected to their respective generator by a matching network. The first jet is fed with varying amounts of argon as a carrier gas mixed with silane (SiH_4) as a reactive precursor gas for particle synthesis, while the second jet can be supplied with additional gases through a cylindrical connector with a symmetric gas feed placed between jets. The gas inlet is designed under an angle of 45° to support the laminar flow inside the jets and to avoid the formation of turbulent vortices, which would lead to a loss of particles. The gas feed for

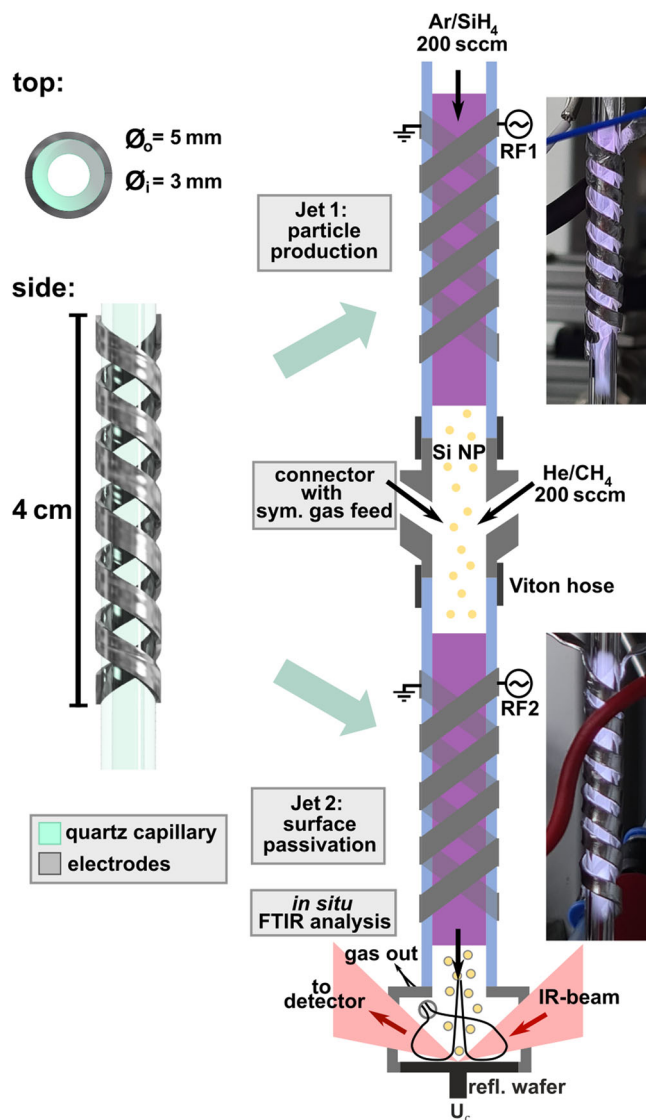


FIGURE 1 | Combined setup of two atmospheric pressure plasma sources connected via a symmetrical gas connector. The first jet is carrying out particle production, and the second one the surface passivation. The resulting particles and the consumption of precursors are monitored using in situ FTIR analysis.

the second jet uses helium as a carrier gas, with the possibility to mix a reactive gas to induce surface passivation.

Si-NCs were synthesized in the first jet using an RF power of 150 W and a gas flow of 200 sccm. The silane concentration was varied between 5 and 50 ppm by mixing pure argon with a fixed mixture of 100 ppm silane in argon. For the surface passivation of Si-NC synthesized in the first jet at a silane concentration of 5 ppm, the second jet has been fed with an additional 200 sccm of 0.05% CH_4 diluted in helium. Helium was chosen as a carrier gas to facilitate the plasma ignition [20] thus allowing for the second jet to be operated in a pulsed mode. To pulse the second generator, a TTL signal (0–5 V) has been utilized with different duty cycles. The pulse width of the signal has been chosen in agreement with the residence time of the particles in the second plasma. For an overall flow of 400 sccm, the average residence time of the particles in the second plasma volume is around 20 ms.

Using appropriate pulsing settings ensures that nanoparticles transitioning through the second plasma should pass through an ignited state at least once in their residence time. The pulse can be operated on different duty cycles to tune the dissociation degree of methane. A duty cycle of 0% corresponds to the second plasma being off (no treatment), while a continuous wave (cw) operation corresponds to a duty cycle of 100%. The generated and treated nanoparticles are carried downstream by the gas flow toward a polished substrate. Here, they are collected on a substrate using a positive bias voltage of $U_c = 3$ kV. Due to the negative charge of the particles, the positive bias results in a particle drift toward the substrate. This is important for the subsequent ex situ measurements as well as for the in situ FTIR analysis.

2.2 | In Situ Fourier Transform Infrared Spectroscopy

The FTIR in this study was carried out using a commercial Bruker VERTEX 80V spectrometer with a wavenumber resolution of 4 cm^{-1} . The IR beam can be coupled out of the spectrometer and then directed into the in situ setup as shown in Figure 2. The beam is focused and reflected by a mirror through a KBr window onto a biased substrate, where the nanoparticles are collected. A reflective substrate (e.g., a polished silicon wafer or stainless steel substrate) is chosen to reflect the IR beam through the second KBr window onto another mirror and then into a liquid-nitrogen-cooled MCT detector. The IR beam is then absorbed by the deposited particles and also in the gas phase inside the small chamber with the substrate, providing additional information about the presence and consumption of molecular precursors. The beam path outside the small chamber is flushed with dry nitrogen gas to ensure a dry environment and to minimize the absorption by CO_2 and H_2O coming from the ambient air. FTIR spectra are post-processed by the subtraction of polynomial background.

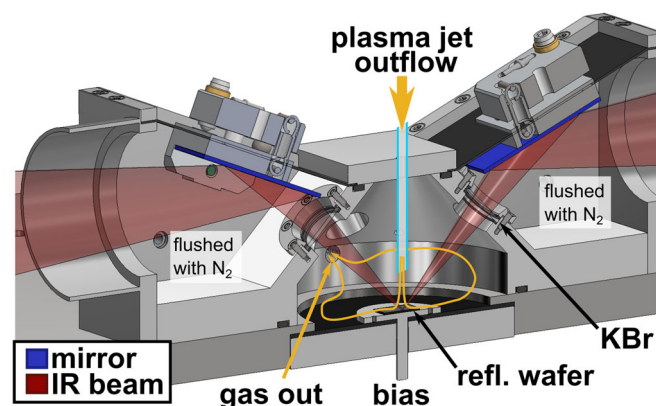


FIGURE 2 | CAD sketch of the in situ FTIR setup. The IR beam is exiting the device and is directed via a mirror onto a reflective wafer. The reflective wafer is placed directly under the outflow of the plasma jet. The beam path is flushed with nitrogen in the outer parts of the chamber; the core chamber is filled with gases exiting the jet.

2.3 | TEM

Direct investigation of particle sizes, morphology, crystal structure, and chemical composition was performed by TEM. In this case, a field emission gun equipped with FEI Tecnai F30 G² STwin operated at 300 kV was used to study nanoparticles in TEM bright field mode. TEM samples were obtained by placing TEM holey carbon copper grids below the output of the jet on a collection electrode that could be positively biased with 3 kV. The local elemental composition was examined by energy-dispersive X-ray (EDX) spectroscopy, providing estimated values of the oxygen concentration. A quantitative determination is beyond the scope of this study. The particle size distribution was calculated from particle diameters measured using the ImageJ software.

2.4 | X-Ray Photo-Electron Spectroscopy (XPS)

XPS was used to study the chemical composition and chemical bonds on the surface of the passivated Si-NPs. Corresponding samples were measured using an XPS UHV system from PRE-VAC Sp. z o. o., equipped with an Al-anode operating at 300 W. Widescans were performed by using three iterations and a pass energy of 200 eV. High-resolution scans were measured with 20 iterations and a pass energy of 50 eV. For the processing and analysis of the XPS spectra, the software CasaXPS (version 2.3.23) was used. The background correction was done by applying the Shirley algorithm [21]. For all recorded spectra, charge correction was applied by setting the C–C representing component in the fitted C 1s spectra of each sample to 284.8 eV.

2.5 | PL Measurements

The steady-state PL spectra were measured directly on the powdered sample using a Shamrock 300i imaging spectrograph (Andor; Oxford Instruments) coupled with a CCD camera. A HeCd laser ($\lambda = 325$ nm; $P = 3.5$ mW) was used to excite the Si-NPs. To minimize the influence of inhomogeneities and laser-induced modification of the sample, the measurement was repeated at different spots on the wafer surface and the collected spectra were compared. All spectra were corrected for the spectral sensitivity of the whole system.

3 | Results and Discussion

The aim of this study is to characterize the effect of plasma treatment on the optical properties of silicon quantum dots. Therefore, the operation parameters of the first jet have been optimized to generate small silicon nanocrystals that exhibit PL behavior. These reference particles can be then modified using the second jet. Particles in the first jet can be generated using argon as a carrier gas. Here, silane concentration, overall gas flow, and applied power are variables. These parameters have a significant influence on the composition and structure of the particles, where the Si-NP sizes usually scale with silane concentration. Residence time and plasma power have a strong effect on the crystallinity.

The TEM images of nanoparticles synthesized at various silane concentrations are shown in Figure 3. As can be expected, a larger concentration leads to larger nanoparticles because there is more material available in the plasma for them to grow. For a silane concentration of 5 ppm, quantum dots with average diameters of around 7.5 nm are formed. Regardless of size, the nanoparticles are crystalline, as indicated by the SAED insets, and have a spherical shape. A detailed study of electron diffraction patterns using rotational averages and their comparison with d -values of cubic silicon showed that the reflections in the SAED patterns correspond to FCC silicon. This shows that the applied power in combination with the selective heating of the nanoparticles [22] is sufficient to reach the crystallization temperature of larger nanoparticles up to 40 nm in diameter. Additionally, all nanoparticles have an amorphous oxygen-rich shell. For the samples from Figure 3, the average diameter as well as the maximum and minimum diameters observed in the TEM images were determined and are shown in Table 1. Using EDX, the atomic concentrations of silicon and oxygen were measured. Both the TEM images and EDX results show that as silane concentration decreases, both the average, and also maximum and minimum diameters of the nanoparticles also decrease. A closer analysis of the average atomic oxygen-to-silicon ratios shows an increase in oxygen content as particle size decreases. This is the consequence of the much larger surface-to-volume ratio of the smaller nanoparticles. Since every nanoparticle has a similar oxygen-rich amorphous shell, smaller particles will inherently exhibit a higher oxygen content, even though the quality of the crystal itself is good.

3.1 | FTIR Results/Particle Composition

Normalized FTIR spectra (measured during the deposition process after 10 min) of the largest and smallest deposited nanoparticles according to Table 1 are plotted in Figure 4. The FTIR band with the greatest peak intensity at around 1100 cm^{-1} corresponds to Si-O-Si bonds and its broad appearance can be explained by the simultaneous excitation of both longitudinal and transversal oscillation modes due to the incident angle of the reflective FTIR setup as explained in Ref [23]. This oxygen contamination results very probably from the residual water molecules in the system, impurities in the process gases, or leak of air into the setup. The wavenumbers in the range of $2100\text{--}2300\text{ cm}^{-1}$ contain the absorption peaks of the Si-H-bonds. Here, a much higher degree of non-oxidized Si-H-bonds is found in the 50 ppm sample of larger nanoparticles.

TABLE 1 | Average d_{avg} and maximum d_{max} diameters for silicon nanoparticles synthesized at different silane concentrations c_{SiH_4} , as well as the elemental compositions of these nanoparticles as determined by EDX.

	c_{SiH_4}	d_{avg} in nm	d_{max}	at% Si	at% O
a	50 ppm	16.3 ± 6.1	40.8 nm	94	6
b	25 ppm	14.5 ± 3.6	24.6 nm	85	15
c	10 ppm	9.3 ± 2.4	16.9 nm	72	28
d	5 ppm	7.4 ± 2.3	14.6 nm	48	52

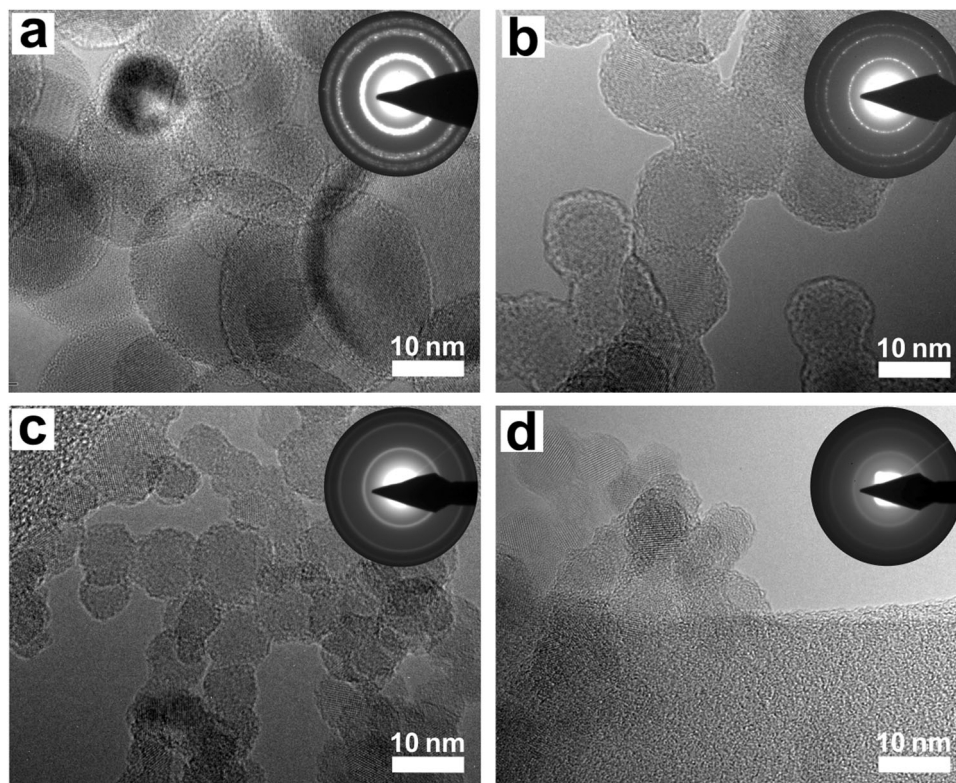


FIGURE 3 | TEM images of nanoparticles synthesized in the first jet at a power of 150 W with a fixed overall flow of 200 sccm at silane admixtures of (a) 50 ppm, (b) 25 ppm, (c) 10 ppm, and (d) 5 ppm.

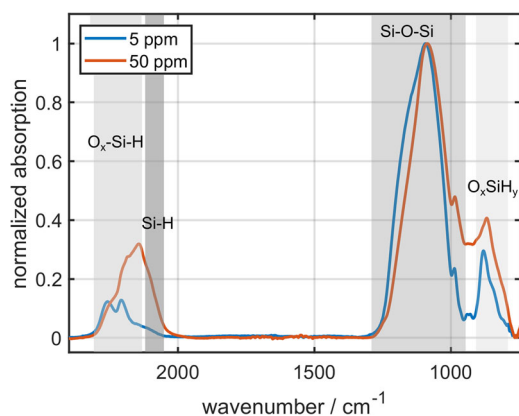


FIGURE 4 | In situ FTIR spectra of silicon nanoparticles generated at a silane admixture of 50 ppm in red and 5 ppm in blue. Applied plasma power was 150 W and the overall gas flow was 200 sccm.

Several factors can contribute to this effect. First, smaller Si-NPs are generated at smaller silane admixtures, where the ratio of silane to impurities is smaller and the oxidation larger. Second, the amount of the available hydrogen per surface site of Si-NPs is larger for larger Si-NPs. The silane molecule is a source of hydrogen in this process with a 4:1 H:Si ratio. Most of the silicon is located in the Si-NP volume for larger particles, leaving more hydrogen available per surface site in the plasma compared to the case of smaller Si-NPs, where much more Si is located at the surface. Moreover, hydrogen is likely located at the particle surface. Smaller particles are heated in the plasma more easily [22], allowing them to reach and stay at temperatures high enough for hydrogen desorption from the amorphous silicon to occur.

4 | Surface Passivation Using Methane

As discussed in the introduction, the passivation of the nanoparticle surface with methyl groups (and, in general, with hydrocarbon chains) can strongly influence the Si-NC optical properties. Therefore, plasma conditions have to be found that will enhance surface passivation with hydrocarbon functional groups, while preventing the fast deposition of a thick hydrocarbon layer. These conditions can be realized by a pulsed plasma operation, reducing the average specific energy per molecule. Mainly CH_3 fragments are generated as primary CH_4 dissociation products under these conditions [24]. The reactivity of CH_3 radicals is negligible in the gas phase [25], and it is rather slow at the surface. Additionally, atomic hydrogen is produced which can generate dangling bonds at the NP surface, to which the CH_3 radicals can attach with a higher probability (around 0.01) as has been observed in the case of their interaction with hydrocarbon films [26]. The low surface reactivity of CH_3 should make surface passivation more probable compared to thin film growth. The smallest crystalline particles synthesized at 5 ppm of silane in argon were selected for subsequent passivation experiments.

4.1 | Methane Consumption

As a first step, methane consumption is monitored by means of FTIR absorption in the gas phase measured at the methane band at a wavenumber of 3014 cm^{-1} in the exhaust gases

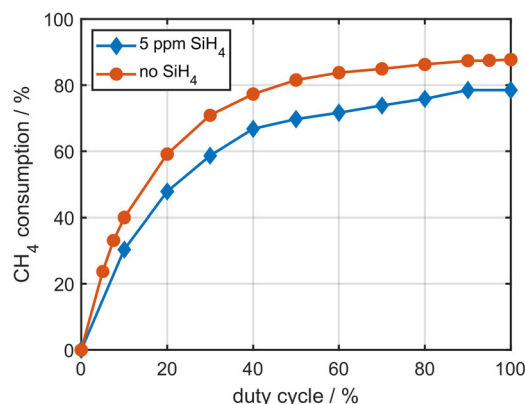


FIGURE 5 | Methane consumption for different duty cycles as measured for the case of particles being synthesized in the first jet (blue) and for the case of no particles produced (red).

coming out of the second plasma jet for its different duty cycles. This is later used as an indicator for the plasma chemistry processes. As can be seen in Figure 5, the consumption of methane in the second jet increases with the length of the duty cycle, as the CH_4 signal in the FTIR measurement becomes weaker, which is an expected result. This trend is consistent regardless of whether the first jet operates with argon alone or with the argon/silane mixture. However, methane consumption is slightly lower when silane is introduced into the first jet. When no silane is admixed (red curve), the maximum methane consumption is slightly higher and less CH_4 is leaving the second jet in the exhaust gases. When introducing silane in the first jet, there is more hydrogen in the system that can etch the amorphous carbon layers on the walls with CH_4 being one of the main etching products, as has been shown in Ref [27]. Additionally, nanoparticles will attract charges making the second plasma weaker. This can change the plasma chemistry. Higher methane dissociation in the second plasma indicates the presence of highly reactive methane fragments (CH_x radicals) that can lead to carbon film or dust formation. Since the aim is to passivate the Si-NC with methyl radicals, only a weak second plasma with lower CH_4 consumption is desirable. Therefore, a duty cycle below 10% should be used in this process as an optimal operation mode.

4.2 | FTIR Analysis of the Surface Passivation

Figure 6 shows the normalized and background-corrected FTIR spectra as measured by the in situ setup for untreated Si-NPs in blue, as well as for particles that were treated with a pulsed (50 Hz) plasma with a 0.05% methane admixture. A duty cycle of $D = 60\%$ is shown in yellow, and a duty cycle of $D = 7.5\%$ is shown in red. The peaks at 1100 and 800 cm^{-1} correspond to asymmetric stretching in Si-O-Si [28–30] and Si-O bending [31], respectively. They appear similar for both treated and untreated samples. In the wavenumber range from 2400 to 2000 cm^{-1} , Si-H_x [32, 33], R-Si-H₃ [34], and O-Si-H [32] bonds can be identified. Here, a treatment at high-duty cycles (yellow) seems to almost completely remove these bonds from the particle surface. Instead, several peaks in the region from 1800 to 1400 cm^{-1} appear, which indicate

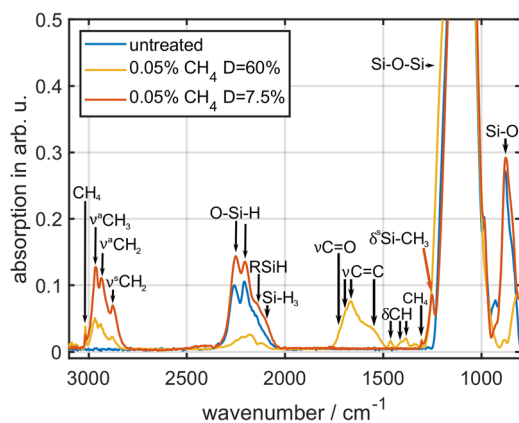


FIGURE 6 | FTIR spectra for nanoparticles synthesized at 5 ppm silane untreated (blue) and treated with 0.05% CH₄ admixture for duty cycles of 60% (yellow) and 7.5% (red). Spectra are shown normalized to the peak at 1100 cm⁻¹.

the formation of a thick hydrocarbon layer on top of the particles produced with duty cycle $D = 60\%$. The peak at 1720 cm⁻¹ can be identified to be C = O stretching vibrations [35]. In the range from 1680 to 1550 cm⁻¹, the stretching vibrations of double-bonded carbon are found [36]. The region from 1450 to 1370 cm⁻¹ includes the deformation vibrations of CH bonds [37].

The growth of a thin amorphous hydrocarbon carbon layer can be identified for all treated samples in the wavenumber region from 3000 to 2800 cm⁻¹, independent of the length of the duty cycle. Here, three peaks can be identified as the asymmetric stretching of CH₃ (2964 cm⁻¹) as well as the asymmetric (2934 cm⁻¹) and symmetric (2880 cm⁻¹) stretching of CH₂ according to Refs [38, 39]. This amorphous hydrocarbon layer is not present in the untreated sample (blue) and is also not observed when the first jet is switched off (not shown here). Therefore, a carbon thin film deposition on the substrate can be excluded and these new features in the spectra are present only due to a carbon film growing on top of the nanoparticles.

The last difference between the three spectra can be observed at a wavenumber of 1260 cm⁻¹. Here, only the sample treated at $D = 7.5\%$ exhibits a peak, which corresponds to the CH₃ deformation vibration in Si-CH₃. [29, 30]. This peak which is not present in the untreated sample can be an indicator for a successful surface passivation with CH₃. This will be further verified with XPS measurements.

Overall, the duration of the duty cycle strongly influences the passivation and termination of the Si-NPs. Untreated nanoparticles first exhibit Si-H bonds at the surface, which then quickly oxidize in ambient air, leaving the surface to be terminated by oxygen. For short duty cycles, a peak at 1260 cm⁻¹ in the FTIR spectra indicates the successful attachment of methyl groups to silicon atoms at the nanoparticle surface, with the additional presence of C-bonded CH₃ and CH₂ groups. For increased duty cycles, a thick carbon layer is probably formed, completely covering the particle and preventing the formation of the other surface bonds as demonstrated by their reduced relative contribution to the absorption spectrum.

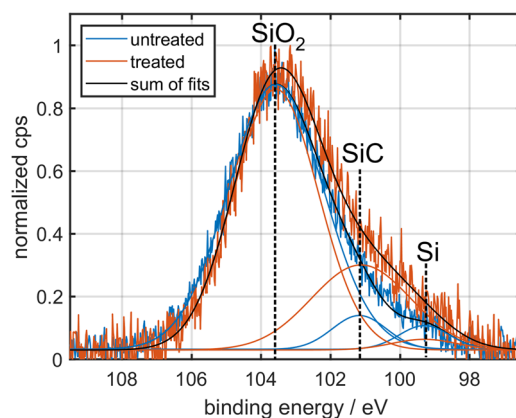


FIGURE 7 | Background-corrected and normalized XPS spectra for an untreated sample in blue and a sample treated with a duty cycle of 7.5% in red.

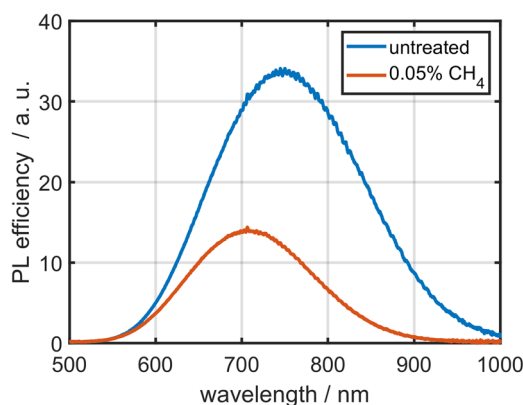


FIGURE 8 | Photoluminescence intensity spectra for nanoparticles synthesized at 5 ppm silane untreated (blue) and treated with 0.05% CH₄ admixture at a duty cycle of $D = 7.5\%$.

4.3 | XPS Results

XPS measurements have been carried out to further investigate the formation of Si-C bonds. Figure 7 shows the background-corrected and normalized spectra for the Si 2p core-level spectrum of an untreated sample (blue) and a sample treated at a duty cycle of $D = 7.5\%$ (red). Additionally, a sum of three Gaussian functions has been fitted to each spectrum. The starting parameters for the maxima of the fits were chosen corresponding to the binding energies for SiO₂ (103.6 eV), SiC (101.0 eV), and Si-Si in lattice silicon (99 eV) [40, 41]. When comparing the graphs and the fits, the treated sample exhibits a more pronounced Si-C peak. Despite the noise, a more prominent low-energy shoulder of the Si 2p peak is clearly visible, suggesting the presence of methyl groups or carbon bound to the surface of the Si-NPs. Together with the in situ FTIR data, this confirms the formation of silicon-carbon bonds and confirms the methylation of the Si NPs in the methane-containing plasma in the second jet.

4.4 | PL

The spectra of the PL measurements can be seen in Figure 8 for the untreated particles in blue, as well as the particles that

underwent treatment with CH₄ containing second plasma in red. All spectra were corrected for the spectral sensitivity of the whole system. Although the setup does not allow for the collection of absolute photoluminescent intensity, the spectra are expected to be comparable. Since nanoparticles of the same size were collected at similar conditions and with similar resulting thin films, the scattering of the excitation laser and the angular radiation of the PL from the sample will be comparable. Additionally, three independent measurements on three different spots of each sample yield similar photoluminescent intensity. Since the primary focus is on the wavelength shift, this shift can be quantitatively expressed. The untreated sample exhibits a strong PL signal with the maximum at a wavelength of 750 nm. In comparison, the sample treated with 0.05% CH₄ at a duty cycle of $D = 7.5\%$ shows a clear blue shift with a maximum at around 710 nm, but at only half the intensity. A similar behavior has already been observed by other research groups, where methylation was able to induce a blue shift in the PL signal, but at the same time reduced the overall PL intensity drastically [42]. Samples produced at duty cycles of 10% were not of optical quality and did not exhibit any PL. This is probably due to the thick CH layer on the particles.

5 | Conclusions

A set-up of two HelixJet plasma sources has been successfully used for the combined synthesis and treatment of Si-NPs with optical properties. TEM measurements revealed that monocrystalline particles of various sizes can be synthesized depending on the silane admixture. For small silane admixtures of around 5 ppm, the particles turned into quantum dots with average diameters of 7 nm exhibiting a PL response visible to the naked eye with a maximum at around 750 nm. When treating these particles with a second identical HelixJet plasma source with an admixture of helium-diluted CH₄ and operated in pulsed mode with variable duty cycle, the appearance of an Si-CH₃ absorption could be observed for a small duty cycle using a custom-built in situ FTIR setup, as well as the growth of an amorphous carbon layer on the silicon particles for duty cycles of 10% and above. For small duty cycles, the successful passivation of silicon with carbon groups could be verified by XPS analysis, where only the treated samples displayed the peak for silicon-carbon bonds. The methane plasma treatment with small duty cycles successfully led to a blue shift in the PL of silicon nanocrystals with the maximum shifted to 710 nm after the treatment.

Acknowledgments

We gratefully acknowledge funding of this project by the German Research Foundation (DFG, project number 426208229) and Major Research Instrumentation Program projects (INST 257/595-1 and INST 257/704-1). The authors would also like to thank Thomas Strunskus for his insights into the evaluation of the XPS data. Open Access funding enabled and organized by Projekt DEAL.

Conflicts of Interest

The authors declare no conflicts of interest.

Data Availability Statement

The data that support the findings of this study are available from the corresponding author upon reasonable request.

References

1. S. P. Low, N. H. Voelcker, L. T. Canham, and K. A. Williams, "The Biocompatibility of Porous Silicon in Tissues of the Eye," *Biomaterials* 30 (2009): 2873–2880, <https://doi.org/10.1016/j.biomaterials.2009.02.008>.
2. A. Fucikova, J. Valenta, I. Pelant, et al., "Silicon Nanocrystals and Nanodiamonds in Live Cells: Photoluminescence Characteristics, Cytotoxicity and Interaction With Cell Cytoskeleton," *RSC Advances* 4 (2014): 10334–10342, <https://doi.org/10.1039/c3ra47574c>.
3. K. Herynková, P. Šimáková, O. Cibulka, A. Fučíková, and M. Hubálek Kalbáčová, "Hydrophilic Luminescent Silicon Nanoparticles in Steric Colloidal Solutions: Their Size, Agglomeration, and Toxicity," *Physica Status Solidi C* 14 (2017): e1700195, <https://doi.org/10.1002/pssc.201700195>.
4. S. Chinnathambi, S. Chen, S. Ganesan, and N. Hanagata, "Silicon Quantum Dots for Biological Applications," *Advanced Healthcare Materials* 3 (2013): 10–29, <https://doi.org/10.1002/adhm.201300157>.
5. X. Ji, H. Wang, B. Song, B. Chu, and Y. He, "Silicon Nanomaterials for Biosensing and Bioimaging Analysis," *Frontiers in Chemistry* 6 (2018): 38, <https://doi.org/10.3389/fchem.2018.00038>.
6. M. Müller, P. Galář, J. Stuchlík, J. Kočka, J. Kupka, and K. Kůsová, "Synthesis and Surface Modification of Light Emitting Silicon Nanoparticles Using Non-Thermal Plasma Techniques," *European Physical Journal Applied Physics* 89 (2020): 20401, <https://doi.org/10.1051/epjap/2020190263>.
7. S. Morozova, M. Alikina, A. Vinogradov, and M. Pagliaro, "Silicon Quantum Dots: Synthesis, Encapsulation, and Application in Light-Emitting Diodes," *Frontiers in Chemistry* 8 (2020): 191, <https://doi.org/10.3389/fchem.2020.00191>.
8. M. Otsuka, Y. Kurokawa, Y. Ding, et al., "Silicon Nanocrystal Hybrid Photovoltaic Devices for Indoor Light Energy Harvesting," *RSC Advances* 10 (2020): 12611–12618, <https://doi.org/10.1039/d0ra00804d>.
9. H. Wang and Y. He, "Recent Advances in Silicon Nanomaterial-Based Fluorescent Sensors," *Sensors* 17 (2017): 268, <https://doi.org/10.3390/s17020268>.
10. B. Chu, H. Wang, B. Song, F. Peng, Y. Su, and Y. He, "Fluorescent and Photostable Silicon Nanoparticles Sensors for Real-Time and Long-Term Intracellular pH Measurement in Live Cells," *Analytical Chemistry* 88 (2016): 9235–9242, <https://doi.org/10.1021/acs.analchem.6b02488>.
11. W. Petasch, B. Kegel, H. Schmid, K. Lendenmann, and H. Keller, "Low-Pressure Plasma Cleaning: A Process for Precision Cleaning Applications," *Surface and Coatings Technology* 97 (1997): 176–181, [https://doi.org/10.1016/S0257-8972\(97\)00143-6](https://doi.org/10.1016/S0257-8972(97)00143-6).
12. L. Holland, "Some Characteristics and Uses of Low-Pressure Plasmas in Materials Science," *Journal of Vacuum Science and Technology* 14 (1977): 5–15, <https://doi.org/10.1116/1.569159>.
13. T. Nozaki, K. Sasaki, T. Ogino, D. Asahi, and K. Okazaki, "Microplasma Synthesis of Tunable Photoluminescent Silicon Nanocrystals," *Nanotechnology* 18 (2007): 235603, <https://doi.org/10.1088/0957-4484/18/23/235603>.
14. K. Kůsová, O. Cibulka, K. Dohnalová, et al., "Brightly Luminescent Organically Capped Silicon Nanocrystals Fabricated at Room Temperature and Atmospheric Pressure," *ACS Nano* 4 (2010): 4495–4504, <https://doi.org/10.1021/nn1005182>.
15. P. Hapala, K. Kůsová, I. Pelant, and P. Jelínek, "Theoretical Analysis of Electronic Band Structure of 2- to 3-nm Si Nanocrystals," *Physical Review B* 87 (2013): 195420, <https://doi.org/10.1103/physrevb.87.195420>.

16. X. D. Pi, R. W. Liptak, S. A. Campbell, and U. Kortshagen, "In-Flight Dry Etching of Plasma-Synthesized Silicon Nanocrystals," *Applied Physics Letters* 91 (2007): e083112, <https://doi.org/10.1063/1.2773931>.
17. L. Mangolini and U. Kortshagen, "Plasma-Assisted Synthesis of Silicon Nanocrystal Inks," *Advanced Materials* 19 (2007): 2513–2519, <https://doi.org/10.1002/adma.200700595>.
18. A. M. Boies, J. T. Roberts, S. L. Girshick, B. Zhang, T. Nakamura, and A. Mochizuki, "SiO₂ Coating of Silver Nanoparticles by Photo-induced Chemical Vapor Deposition," *Nanotechnology* 20 (2009): 295604, <https://doi.org/10.1088/0957-4484/20/29/295604>.
19. J. Schäfer, A. Quade, K. J. Abrams, et al., "HelixJet: An Innovative Plasma Source for Next-Generation Additive Manufacturing (3D Printing)," *Plasma Processes and Polymers* 17 (2020): 1900099, <https://doi.org/10.1002/ppap.201900099>.
20. S. P. Das, G. Dalei, and A. Barik, "A Dielectric Barrier Discharge (DBD) Plasma Reactor: An Efficient Tool to Measure the Sustainability of Non-Thermal Plasmas Through the Electrical Breakdown of Gases," *IOP Conference Series: Materials Science and Engineering* 410 (2018): 012004, <https://doi.org/10.1088/1757-899x/410/1/012004>.
21. D. A. Shirley, "High-Resolution X-Ray Photoemission Spectrum of the Valence Bands of Gold," *Physical Review B* 5 (1972): 4709–4714, <https://doi.org/10.1103/physrevb.5.4709>.
22. L. Mangolini and U. Kortshagen, "Selective Nanoparticle Heating: Another Form of Nonequilibrium in Dusty Plasmas," *Physical Review E* 79 (2009): 1–8, <https://doi.org/10.1103/PhysRevE.79.026405>.
23. T. de los Arcos, H. Müller, F. Wang, et al., "Review of Infrared Spectroscopy Techniques for the Determination of Internal Structure in Thin SiO₂ Films," *Vibrational Spectroscopy* 114 (2021): 103256, <https://doi.org/10.1016/j.vibspec.2021.103256>.
24. S. Ravasio and C. Cavallotti, "Analysis of Reactivity and Energy Efficiency of Methane Conversion Through Non-Thermal Plasmas," *Chemical Engineering Science* 84 (2012): 580–590, <https://doi.org/10.1016/j.ces.2012.09.012>.
25. W. A. Pryor, D. L. Fuller, and J. P. Stanley, "Reactions of Radicals. 41. Reactivity Patterns of the Methyl Radical," *Journal of the American Chemical Society* 94 (1972): 1632–1638, <https://doi.org/10.1021/ja00760a034>.
26. A. von Keudell, "Formation of Polymer-Like Hydrocarbon Films From Radical Beams of Methyl and Atomic Hydrogen," *Thin Solid Films* 402 (2002): 1–37, [https://doi.org/10.1016/s0040-6090\(01\)01670-4](https://doi.org/10.1016/s0040-6090(01)01670-4).
27. J. Benedikt, "Plasma-Chemical Reactions: Low Pressure Acetylene Plasmas," *Journal of Physics D: Applied Physics* 43 (2010): 043001, <https://doi.org/10.1088/0022-3727/43/4/043001>.
28. G. Socrates, *Infrared and Raman Characteristic Group Frequencies: Tables and Charts*, 3rd ed. (Chichester: John Wiley & Sons Inc., 2004).
29. L. M. Johnson, L. Gao, C. W. Shields, IV, et al., "Elastomeric Microparticles for Acoustic Mediated Bioseparations," *Journal of Nanobiotechnology* 11 (2013): 22, <https://doi.org/10.1186/1477-3155-11-22>.
30. V. Raballand, J. Benedikt, J. Wunderlich, and A. von Keudell, "Inactivation of *Bacillus atrophaeus* and of *Aspergillus niger* Using Beams of Argon Ions, of Oxygen Molecules and of Oxygen Atoms," *Journal of Physics D: Applied Physics* 41 (2008): 115207, <https://doi.org/10.1088/0022-3727/41/11/115207>.
31. J. Serra, P. González, S. Liste, et al., "FTIR and XPS Studies of Bioactive Silica Based Glasses," *Journal of Non-Crystalline Solids* 332 (2003): 20–27, <https://doi.org/10.1016/j.jnoncrysol.2003.09.013>.
32. P. Gupta, A. Dillon, A. Bracker, and S. George, "FTIR Studies of H₂O and D₂O Decomposition on Porous Silicon Surfaces," *Surface Science* 245 (1991): 360–372, [https://doi.org/10.1016/0039-6028\(91\)90038-t](https://doi.org/10.1016/0039-6028(91)90038-t).
33. Y. Ogata, H. Niki, T. Sakka, and M. Iwasaki, "Hydrogen in Porous Silicon: Vibrational Analysis of SiH_x Species," *Journal of the Electrochemical Society* 142 (1995): 195–201, <https://doi.org/10.1149/1.2043865>.
34. D. A. Long, "Infrared and Raman Characteristic Group Frequencies. Tables and Charts George Socrates John Wiley and Sons, Ltd, Chichester, Third Edition, 2001. Price €135," *Journal of Raman Spectroscopy* 35 (2004): 905, <https://doi.org/10.1002/jrs.1238>.
35. M. Clin, O. Durand-Drouhin, A. Zeinert, and J. Picot, "A Correlation Between the Microstructure and Optical Properties of Hydrogenated Amorphous Carbon Films Prepared by RF Magnetron Sputtering," *Diamond and Related Materials* 8 (1999): 527–531, [https://doi.org/10.1016/s0925-9635\(98\)00404-x](https://doi.org/10.1016/s0925-9635(98)00404-x).
36. V. Chhabra, K. Bambery, S. Bhattacharya, and Y. Shastri, "Thermal and in Situ Infrared Analysis to Characterise the Slow Pyrolysis of Mixed Municipal Solid Waste (MSW) and Its Components," *Renewable Energy* 148 (2020): 388–401, <https://doi.org/10.1016/j.renene.2019.10.045>.
37. P. K. Chu and L. Li, "Characterization of Amorphous and Nanocrystalline Carbon Films," *Materials Chemistry and Physics* 96 (2006): 253–277, <https://doi.org/10.1016/j.matchemphys.2005.07.048>.
38. P. Couderc and Y. Catherine, "Structure and Physical Properties of Plasma-Grown Amorphous Hydrogenated Carbon Films," *Thin Solid Films* 146 (1987): 93–107, [https://doi.org/10.1016/0040-6090\(87\)90343-9](https://doi.org/10.1016/0040-6090(87)90343-9).
39. B. Dischler, A. Bubenzer, and P. Koidl, "Hard Carbon Coatings With Low Optical Absorption," *Applied Physics Letters* 42 (1983): 636–638, <https://doi.org/10.1063/1.94056>.
40. D. S. Jensen, S. S. Kanyal, N. Madaan, et al., "Silicon (100)/SiO₂ by XPS," *Surface Science Spectra* 20 (2013): 36–42, <https://doi.org/10.1116/11.20121101>.
41. G. Ervin, "Oxidation Behavior of Silicon Carbide," *Journal of the American Ceramic Society* 41 (1958): 347–352, <https://doi.org/10.1111/j.1151-2916.1958.tb12932.x>.
42. P. Galáf, J. Stuchlík, M. Müller, J. Kočka, and K. Kůsová, "Highly Spherical SiC Nanoparticles Grown in Nonthermal Plasma," *Plasma Processes and Polymers* 19 (2021): e2100127, <https://doi.org/10.1002/ppap.202100127>.